Phases in the Al-Corner of the Al–Mn–Be System

Franc Zupanič,[1,*] Boštjan Markoli,[2] Iztok Naglič,[2] Tobias Weingärtner,[3] Anton Meden,[4] and Tonica Bončina[1]

[1]*Faculty of Mechanical Engineering, University of Maribor, Smetanova ulica 17, SI-2000 Maribor, Slovenia*
[2]*Faculty of Natural Sciences and Engineering, University of Ljubljana, Aškerčeva 12, SI-1000, Slovenia*
[3]*Institute for Applied Materials – Applied Materials Physics (IAM-AWP), Karslruhe Institute of Technology (KIT), Herrmann-von-Helmholtz-Platz 1, 76344 Eggenstein-Leopoldshafen, Germany*
[4]*Faculty of Chemistry and Chemical Technology, University of Ljubljana, Aškerčeva 5, SI-1000 Ljubljana, Slovenia*

Abstract: This work studied the phases in the Al corner of the Al–Mn–Be phase diagram in the as-cast state and heat-treated conditions. Metallographic investigations, X-ray diffraction, scanning electron microscopy, and energy-dispersive spectroscopy were used for identifying the phases. The Be contents in the identified phases were precisely determined using Auger electron spectroscopy. The results indicated that Al_6Mn does not dissolve Be, whilst λ-Al_4Mn dissolves up to 7 at.% Be. The average composition of the T phase, which is normally designated as $Al_{15}Mn_3Be_2$, was 72 at.% Al, 19 at.% Mn, and 9 at.% Be. The phase with the nominal composition Be_4AlMn contained more Al than Mn. The atomic ratio Al:Mn was between 1.3:1 and 2:1. The hexagonal Be-rich phase did not dissolve any Al and Mn. The icosahedral quasicrystalline (IQC) phase contained up to 45 at.% Be. The compositions of T phase, λ–Al_4Mn, IQC, and Be_4AlMn may vary, however, the ratio (Al + Be):Mn remained constant, and was close either to four or six indicating substitution of Al atoms with Be atoms in these phases.

Key words: intermetallic phases, aluminum, manganese, beryllium, XRD, AES

Introduction

The Al–Mn–Be alloys represent a starting point for quasicrystal-strengthened Al alloys. Namely, it was found that Be strongly increases the quasicrystal-forming ability of the Al–Mn alloys; thus quasicrystals can appear at those cooling rates attainable using conventional and advanced casting techniques (Kim et al., 2002). Cast and wrought alloys with different fractions of quasicrystals can be produced. The strength of such an alloy compares well to the strength of standard high-strength aluminum alloys, simultaneously retaining considerable ductility (Markoli et al., 2012).

Within these alloys, several other phases can form next to a metastable icosahedral quasicrystalline (IQC) phase. It should be stressed that many of these phases, including IQC, consist of atomic clusters as "building entities." However, the clusters are not isolated entities as they may interpenetrate each other (Trambly de Laissardière et al., 2005). There are no intermetallic phases in the Al–Be phase diagram (Murray & Kahan, 1990; Pan et al., 2004); thus the majority of phases arise from the binary Al–Mn phase diagram (Grushko & Balanetskyy, 2008; Shukla & Pelton, 2009). Nevertheless, some ternary phases were also found (Raynor et al., 1953; Carrabine, 1963). These are all collated in Table 1. A brief overview regarding the origin and designation of phases in Al–Mn, Al–Be, and Al–Mn–Be system will be given in the text below.

In the Al–Mn binary phase diagram, there are two hexagonal structures with large unit cells, the λ-Al_4Mn and the μ-$Al_{4.12}Mn$ (McAlister & Murray, 1990; Trambly de Laissardière et al., 2005; Grushko & Balanetskyy, 2008; Shukla & Pelton, 2009). Phase μ-$Al_{4.12}Mn$ crystallizes close to the composition of the icosahedral phase. This phase is formed via a peritectic reaction around 923°C and is stable down to room temperature. The λ-phase is considered to be closely related to the Al–Mn IQC phase, and is only stable below 722°C. $Al_{11}Mn_4$ (LT), $Al_{11}Mn_4$ (HT), π-Al_4Mn and φ-$Al_{10}Mn_3$ were also reported (Trambly de Laissardière et al., 2005). In addition to these phases, there are also two more intermetallic phases within the Al-rich corner of the Al–Mn phase diagram, namely Al_6Mn and $Al_{12}Mn$ (Shukla & Pelton, 2009).

In the ternary Al–Mn–Be system Raynor et al. (1953) reported a ternary compound called T phase, with an approximate composition of $Al_{15}Mn_3Be_2$. More recently, Kim et al. (2002) discovered two intermetallic phases H1 and H2 with hexagonal crystal structures. They stated that the H1 phase is the Raynor's T phase. Boncina et al. (2009) investigated the $Al_{86}Mn_3Be_{11}$ alloy cast into a copper mould. They found that Be_4AlMn was also present in the alloy, in addition to IQC and H1 phases. The compositions of the phases were also determined by using Auger electron spectroscopy (AES; Zupanic et al., 2013).

As can be seen from Table 1, several stable and metastable phases with large unit cells and cluster substructures can be present, with atomic Al:Mn ratios ranging from 3:1 to 4:1. This can easily lead to misinterpretation of the experimental results and uncertainty in explanation. The complexity increases by the addition of other elements. This is particularly true when an alloying element has a very low atomic number, and so cannot be easily detected and quantified using typical microanalytical methods, such as energy-

*Corresponding author. E-mail: franc.zupanic@um.si

Table 1. Phases Found in the Al-Rich Corner of Al–Mn, Al–Be, and Al–Mn–Be Alloys.

Phase	Crystallographic Data	Source
λ-Al_4Mn	$P6_3/m$, a = 2,8382 nm, c = 1,2389 nm	ICSD #55638
μ-$Al_{4.12}Mn$	$P6_3/mmc$, a = 1.9980 nm, c = 2.4673 nm	ICSD #57971
$Al_{78}Mn_{22}$	*Cmcm*, a = 2.41 nm, b = 3.22 nm, c = 2.40 nm	Trambly de Laissardière et al. (2005)
π-Al_4Mn	*Cmcm*, a = 0.77 nm, b = 3.22 nm, c = 1.24 nm	Trambly de Laissardière et al. (2005)
Al_3Mn	*Pnma*, a = 1.483 nm, b = 1.243 nm, c = 1.251 nm	Trambly de Laissardière et al. (2005)
Al_3Mn	*Pbnm*, a = 1.259 nm, b = 1.480 nm, c = 1.242 nm	Pdf number: 000-26-0028
φ-$Al_{10}Mn_3$	$P6_3/mmc$, a = 0.7543 nm, b = 0.7898 nm	Pdf number: 000-65-2067
$Al_{11}Mn_4$	*P*-1, a = 0.5052 nm, b = 0.8873 nm, c = 0.5034 nm α = 89.7, β = 99.8, γ = 104.9	Pdf number: 000-71-1765
Al_6Mn	*Cmcm*, a = 0.75518 nm, b = 0.64978 nm, c = 0.88703 nm	Pdf number: 000-65-7156
H1	a = 1.2295 nm, c = 2.4634 nm, $P6_3/mmc$	Kim et al. (2002)
H2	a = 1.2295 nm, c = 1.2317 nm, $P6/mmm$	Kim et al. (2002)
T ($Al_{15}Mn_3Be_2$)	Undefined	Raynor et al. (1953)
Be_4AlMn	a = 0.611 nm, *Fd*-3*m*	Pdf number: 000-18-0007
IQC	a = 0.46 nm	Kim et al. (2002)
Al	a = 0.40497 nm, *Fm*-3*m*	Pdf number: 000-65-2869
Be_2Mn	a = 0.4240 nm, c = 0.6923 nm, $P6_3/mmm$	Pdf number: 000-65-3564
$Be_{12}Mn$	a = 0.726 nm, c = 0.4256 nm, $I4/mmm$	Pdf number: 000-42-0901
α-Be	a = 0.22859 nm, c = 0.35844 nm, $P6_3/mmc$	Pdf number: 000-22-0111

IQC, icosahedral quasicrystalline phase.

dispersive spectroscopy (EDS) and wavelength dispersive spectroscopy. Therefore, the main aim of this study was to determine the compositions of phases with much higher precision than those already reported. This was achieved by the use of thorough qualitative and quantitative AES, combined with complementary characterization techniques, such as scanning electron microscopy, EDS, and X-ray diffraction (XRD).

Experimental

The alloys were prepared from pure aluminum (99.997% Al), manganese (99.9% Mn), and beryllium (99.97% Be) using an arc-melting furnace (Compact Arc Melter MAM-1; Edmund Bühler GmbH, Hechingen, Germany) within an argon atmosphere. Chemical composition of the investigated alloys were determined using inductively coupled plasma-atomic emission spectroscopy (Table 2).

Arc-melted alloys were heat-treated within quartz argon filled ampullae at 600, 660, and 750°C for 24 h, 168 h (1 week), and 720 h (1 month). Those samples annealed at 750°C were additionally placed into an aluminum crucible because they had partially melted. The alloy $Al_{92.5}Mn_3Be_{4.5}$ was cast into a 300-μm-thick copper mould in order to obtain an IQC phase.

The samples were investigated using scanning electron microscopy (SIRION NC, FEI, Eindhoven, The Netherlands), EDS (Inca 350, Oxford Instruments, Abingdon, Oxfordshire, UK), AES (PHI 680 Auger Nanoprobe, PHI, Chanhassen, MN, USA), and XRD. XRD was carried out using monochromatic synchrotron radiation with a wavelength of 0.1 nm, at Elettra, Sincrotrone Trieste, Italy. A diffracted beam was recorded using a Dectris Pilatus 2M detector, and LaB_6 was used for calibrating the image. This image was then integrated using Fit2D. Lattice parameters of the LaB_6 were determined using CheckCell and deviated by $<$0.08% from the theoretical values.

Table 2. Chemical Compositions of the Investigated Alloys.

Sample	Unit	Al	Mn	Be
$Al_{97.3}Mn_{1.9}Be_{0.8}$	mass%	96.99	3.75	0.26
	at.%	97.35	1.86	0.79
$Al_{79}Mn_{17}Be_4$	mass%	68.71	30.07	1.22
	at.%	78.89	16.92	4.19
$Al_{75}Mn_{15}Be_{10}$	mass%	69.78	27.01	3.21
	at.%	75.35	14.30	10.35
$Al_{66}Mn_4Be_{30}$	mass%	77.93	10.22	11.85
	at.%	65.85	4.23	29.92
$Al_{92.5}Mn_3Be_{4.5}$	mass%	92.5	6.0	1.5
	at.%	92.5	3.0	4.5
$Al_{85}Be_{15}$	mass%	94.5	—	5.5
	at.%	85.0	—	15.0
$Al_{89}Mn_{11}$	mass%	80.0	20.0	—
	at.%	89.0	11.0	—

Chemical compositions of the phases were determined using EDS and AES. The major drawback of EDS was that it could hardly detect Be in these alloys. The fluorescence yield of Be is very low, and the absorption of Be radiation in a sample is extremely strong (Goldstein et al., 1981). Most of the phases could be analyzed at 15 and 20 kV as they were large enough. However, only the contents of Al and Mn could be accurately measured. Beryllium was determined only qualitatively in the α-Be and Be_4AlMn at lower accelerating voltages of 2 and 3 kV. These voltages were, however, too low to excite Al and Mn atoms.

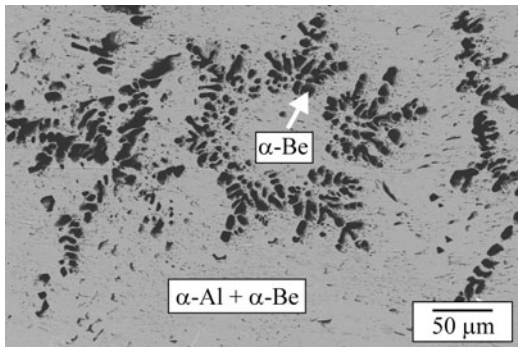

Figure 1. Backscattered electron micrograph of the alloy $Al_{85}Be_{15}$ in the as-cast condition.

AES measurements were carried out at 1×10^{-7} Pa, at a 5 kV accelerating voltage. The electron beam current was 10 nA, and the beam size was close to 24 nm. The sample was tilted 30° from the surface normal to electron gun during acquisition. An Ar ion beam was used for sputter etching with an ion current of 500 nA. Only a few minutes were usually enough for removing the C and O contaminants from the surface. Peak-to-peak height measurements from the derivative spectra were used for quantitative analysis. The accuracies of such measurements are typically around ±20% (Doyle & McDaniel, 2003). In order to improve the measurement accuracy, a 50-μm-thick melt-spun ribbon was used with a uniform microstructure consisting of nanoscale icosahedral particles in an Al-rich matrix. It had the following composition: 88.6 at.% Al, 5.6 at.% Mn and 5.8 at.% Be. Using the empirical procedure, the sensitivity factors of Be, Al, and Mn were determined: $sf(\mathrm{Be}) = 0.168$, $sf(\mathrm{Al}) = 0.066$, and $sf(\mathrm{Mn}) = 0.190$. The chemical composition of the stoichiometric Al_6Mn was determined using these factors. It was revealed that the Al content was determined with an accuracy of ±2%, and that of Mn with accuracy of ±10%. Analysis of the stoichiometric Be_4AlMn revealed that Be in a high concentration range can be determined with an accuracy of ±3%, whilst the contents of Al and Mn were determined with an accuracy of ±10%. The reproducibility of results by the AES analysis of the same phase in a sample was high because standard deviations were often below 1 at.%. Some scattering was found between the different samples, which can be attributed to slight variations in surface conditions.

Results and Discussion

In this part, microstructures and phases found within the binary Al–Be and Al–Mn alloys are presented first. Thereafter, other stable and metastable phases are introduced as found to date in the Al–Mn–Be system. Special attention is devoted to analyzing those phases using AES, and correspondingly to the Be contents in these phases.

Binary Al–Be Alloy

Figure 1 shows a backscattered electron micrograph of the alloy $Al_{85}Be_{15}$. This alloy is a hypereutectic alloy because the eutectic point in the Al–Be phase diagram lies at 2.4 at.% Be. Thus, it consisted of primary α-Be with a typical dendritic morphology, which is characteristic for phases with low melting entropy. The matrix represented the binary α-Al + α-Be eutectic. Eutectic α-Al prevailed, whilst the minor α-Be possessed a rod-like shape due to its very low volume fraction.

EDS, carried out using low accelerating voltages (2 and 3 kV), clearly resolved the Be–K peak positioned at 0.11 keV in α-Be. At these voltages, the Al–K peak cannot appear in the spectrum. Even when using a method as sensitive as AES, no Al peak was observed, indicating that the Al content in αBe was lower than its detection limit, which confirmed that the solubility of Al in Be is negligible. Also in α-Al no Be was detected either with EDS or AES, despite the fact that Al can dissolve up to 0.3 at.% Be (Murray & Kahan, 1990).

Binary Al–Mn Alloy

As stated in the introduction, various phases arising from the binary Al–Mn system can also appear in Al–Mn–Be alloys. In order to demonstrate the complexity of the system, and the difficulties in identifying Al–Mn phases, three microstructures are shown that originated from different processing conditions for the $Al_{89}Mn_{11}$ alloy (Fig. 2). Their corresponding diffraction patterns are presented in Figure 3.

Very slow cooling from 750°C resulted in a microstructure that consisted of predominantly Al_6Mn and α-Al phase (Fig. 2a). EDS and AES revealed that the chemical composition of the bright phase inside Al_6Mn corresponded to Al_4Mn. Its peaks were undetected by XRD due to the small fraction of this phase (Fig. 3, bottom curve). Quenching from 750°C prevented the formation of Al_6Mn (Fig. 2b). The XRD results revealed that the bright phase present within the microstructure at room temperature was λ-Al_4Mn (Fig. 3, top curve). The alloy cast from a temperature above the liquidus line solidified under a cooling rate of about 10 K/s and the phase identified using EDS and AES was Al_4Mn. This phase was enveloped with a thin layer of Al_6Mn (Fig. 2c). The analysis of the corresponding XRD trace revealed that the peak positions did not match any of the known phases in the Al–Mn system (Fig. 3, middle curve). Thus, under specific solidification conditions, metastable phases form other than those already discovered can form.

Ternary Alloys

Figure 4 shows the XRD traces of ternary alloys in the selected states. Their phase compositions, determined using XRD and other metallographic techniques, are given in Table 3. All phases are also labeled in the corresponding micrographs (Figs. 5–9). The detailed AES spectra of all phases for Be, Mn, and Al peaks are depicted in Fig. 10. The alloy $Al_{97.3}Mn_{1.9}Be_{0.8}$ was present in the as-cast state from Al_6Mn and Be_4AlMn. However, during heat treatment Al_6Mn was replaced by λ-Al_4Mn (Fig. 5). In the as-cast condition of

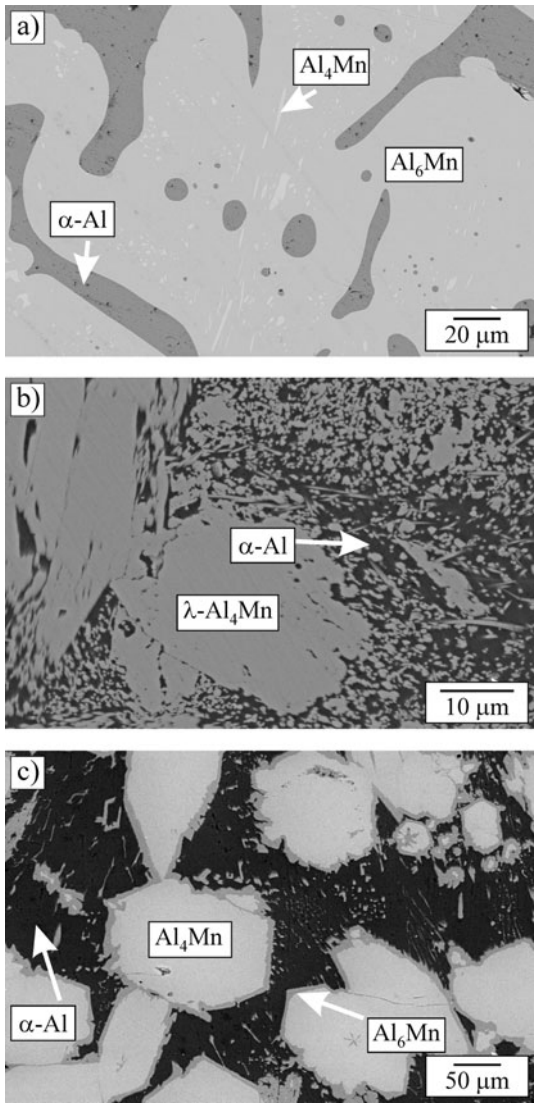

Figure 2. Microstructure of the alloy $Al_{89}Mn_{11}$: (**a**) after annealing at 750°C and slow cooling, (**b**) after annealing at 750°C and water quenching, and (**c**) after casting from the liquid state.

the alloy $Al_{79}Mn_{17}Be_4$, a high-temperature phase $Al_{11}Mn_4$ was present. Upon heat treatment, this phase transformed to stable Al_6Mn while λ-Al_4Mn remained (Fig. 6). Microstructure of the $Al_{75}Mn_{15}Be_{10}$ alloy was almost the same in the as-cast and heat-treated conditions. In this alloy, T phase appeared alongside Be_4AlMn (Fig. 7). The alloy $Al_{66}Mn_4Be_{30}$ consisted of Be_4AlMn and α-Be (Fig. 8). In the as-cast condition, α-Be possessed dendritic morphology. In addition, α-Be was also a part of a binary eutectic (α-Al + α-Be). Upon heat treatment dendritic α-Be remelted, and the melt was in equilibrium only with Be_4AlMn. During quenching, Be_4AlMn remained unchanged while liquid transformed into the binary eutectic (α-Al + α-Be) while no primary dendritic α-Be formed. IQC was only in the as-cast condition of the alloy $Al_{92.5}Mn_3Be_{4.5}$ (Fig. 9). During heat treatment, it decomposed to other phases, predominantly in λ-Al_4Mn and Be_4AlMn, and its microstructure was similar to that of $Al_{97.3}Mn_{1.9}Be_{0.8}$ in Figure 5b.

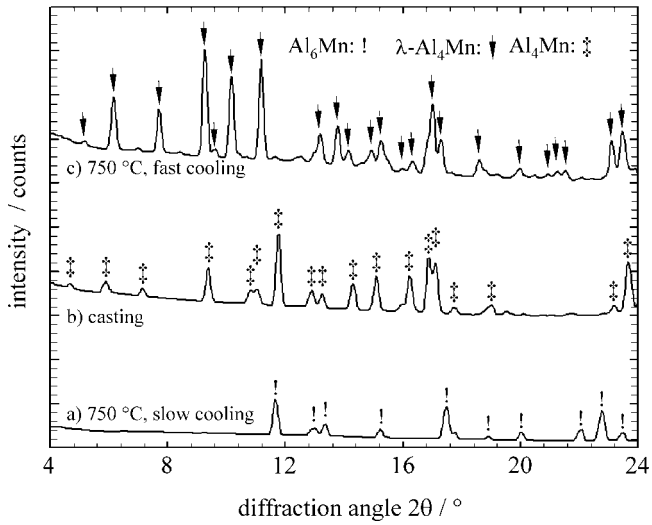

Figure 3. X-ray diffraction traces of $Al_{89}Mn_{11}$: (**a**) after annealing at 750°C and slow cooling, (**b**) after casting from the liquid phase, and (**c**) after annealing at 750°C and water quenching.

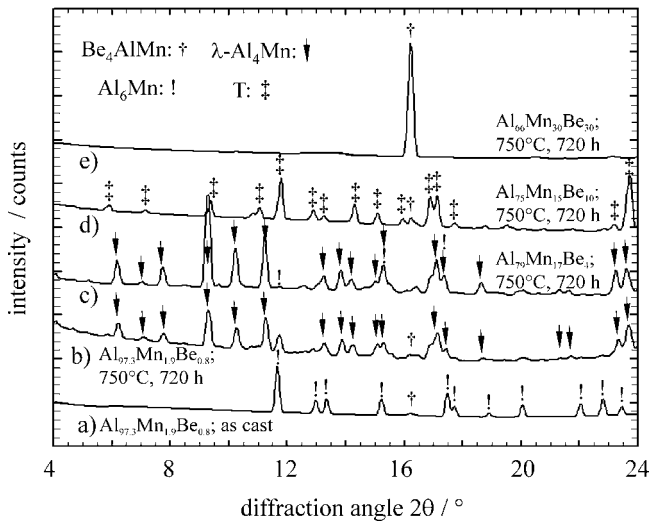

Figure 4. X-ray diffraction traces of the (**a**) $Al_{97.3}Mn_{1.9}Be_{0.8}$, as-cast; (**b**) $Al_{97.3}Mn_{1.9}Be_{0.8}$, 750°C, 720 h; (**c**) $Al_{79}Mn_{17}Be_4$, 750°C, 720 h; (**d**) $Al_{75}Mn_{15}Be_{10}$, 750°C, 720 h; and (**e**) $Al_{66}Mn_4Be_{30}$, 750°C, 720 h.

The results clearly indicate that no phases from the Be–Mn system appeared in the ternary alloys (Okamoto & Tanner, 1990). Neither did phases such as μ-$Al_{4.12}Mn$, $Al_{12}Mn$, and other metastable crystalline phases appear within the investigated alloys. $Al_{11}Mn_4$ was only in the as-cast condition of the alloy $Al_{79}Mn_{17}Be_4$, and IQC only within the fast-cooled alloy $Al_{92.5}Mn_3Be_{4.5}$. The aluminum-rich solid solution (α-Al) was in all alloys, whereas the Be-rich solid solution (α-Be) was only present within alloy $Al_{66}Mn_4Be_{30}$. Al_6Mn and λ-Al_4Mn were present in the alloys with the smaller Be content, i.e., close to the Al–Mn boundary system. Be_4AlMn was only absent in the alloy $Al_{79}Mn_{17}Be_4$, which is close to the Al–Mn system. The T phase was present under all conditions for the alloy $Al_{75}Mn_{15}Be_{10}$, but only in the as-cast state of the alloy

Table 3. Phases Present within the Investigated Ternary Alloys.

Alloy	As-Cast	600°C	660°C	750°C
$Al_{97.3}Mn_{1.9}Be_{0.8}$	Al_6Mn, α-Al, Be_4AlMn, very small fraction T-phase	α-Al, λ-Al_4Mn, Be_4AlMn	—	—
$Al_{79}Mn_{17}Be_4$	$Al_{11}Mn_4$, λ-Al_4Mn, α-Al	—	α-Al, Al_6Mn, λ-Al_4Mn	α-Al, λ-Al_4Mn
$Al_{75}Mn_{15}Be_{10}$	T, Be_4AlMn, α-Al	—	T, Be_4AlMn, α-Al	T, Be_4AlMn, α-Al
$Al_{66}Mn_4Be_{30}$	α-Al, Be_4AlMn, α-Be	α-Al, Be_4AlMn, α-Be	α-Al, Be_4AlMn, α-Be	α-Al, Be_4AlMn
$Al_{92.5}Mn_3Be_{4.5}$	α-Al, IQC	—	—	—

IQC, icosahedral quasicrystalline phase.

$Al_{97.3}Mn_{1.9}Be_{0.8}$. Further detailed characteristics of single phases are given below.

Al-Rich Solid Solution α-Al

α-Al is usually formed upon quenching from those regions consisting of liquid and one or two intermetallic phases. Thus, its composition should correspond to the chemical composition at particular temperatures. Mn peaks were clearly visible with EDS and Mn content was close to the maximum solubility in Al (e.g., around 1 at.%). However, no Be was detected. The contents of Be and Mn were below their detection limits for the AES. The lattice parameters of α-Al were up to 1.5% lower than that of pure Al. This could be attributed to the presence of Mn in the solid solution because its atomic diameter is almost 5% smaller than the aluminum atomic diameter. Be has a 22% smaller diameter, but its solubility in α-Al is too small to have any effect on the aluminum lattice parameter.

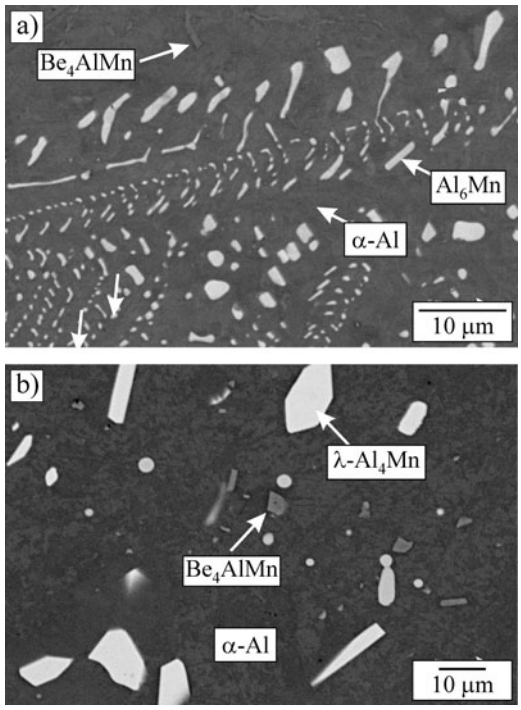

Figure 5. Backscattered electron micrographs of the alloy $Al_{97.3}Mn_{1.9}Be_{0.8}$: (**a**) in the as-cast state and (**b**) after annealing at 600°C for 1 month.

Be-Rich Solid Solution α-Be

Both EDS and AES failed to detect Al and Mn in α-Be. Thus, their solubility in α-Be has to be extremely low. This was also supported by the XRD analyses. The lattice parameters of α-Be differed by $<0.2\%$ from that in Table 1. These deviations were within the range of accuracy for the XRD method.

Al_6Mn

The atomic ratios Al:Mn were close to 6:1 in both alloys, in which Al_6Mn was present. AES for the Al_6Mn clearly showed that the content of Be was below the detection limit (Fig. 10). Thus, the solubility of Be in Al_6Mn must be negligible. In addition, the lattice parameters of Al_6Mn differed by $<0.1\%$ from the lattice parameters of Al_6Mn within crystallographic databases (Table 1).

λ-Al_4Mn

EDS was unable to detect any Be in λ-Al_4Mn. Using quantitative analysis, the ratio Al:Mn was found to be close to

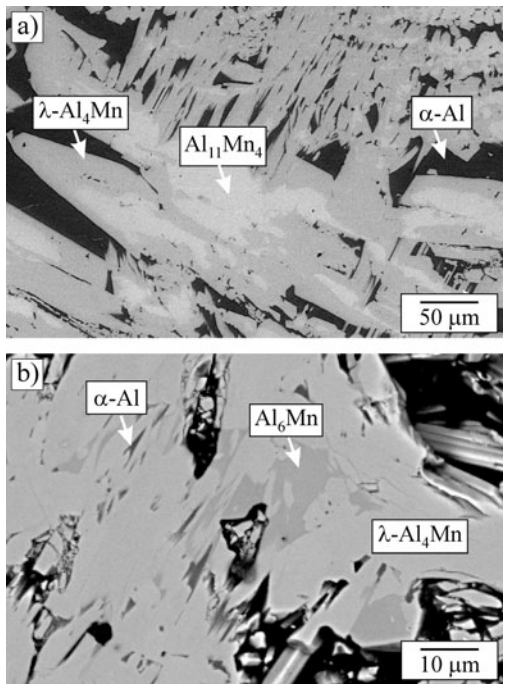

Figure 6. Microstructure of the alloy $Al_{79}Mn_{17}Be_4$: (**a**) in the as-cast state and (**b**) after annealing at 660°C for 1 month.

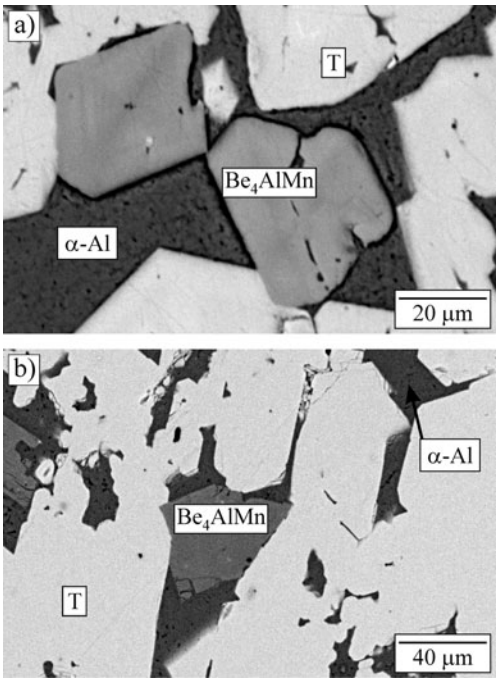

Figure 7. Backscattered electron micrograph of the alloy $Al_{75}Mn_{15}Be_{10}$: (**a**) in the as-cast state and (**b**) annealing at 660°C for 1 month.

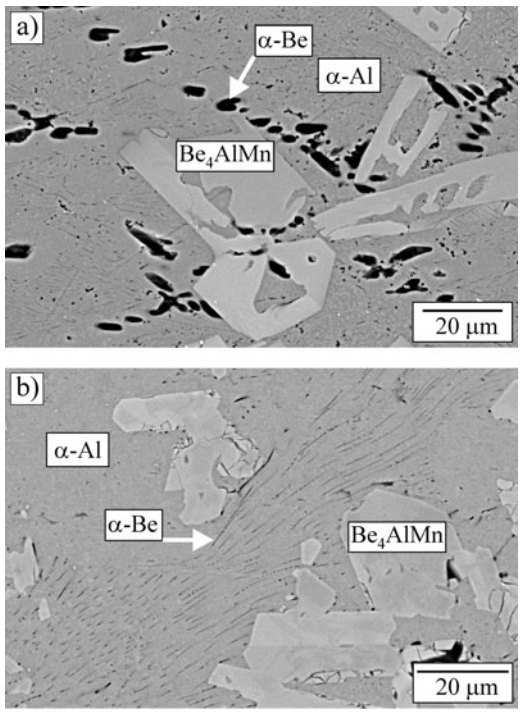

Figure 8. Microstructure of the alloy $Al_{66}Mn_4Be_{30}$: (**a**) in the as-cast state and (**b**) after annealing at 750°C for 1 month.

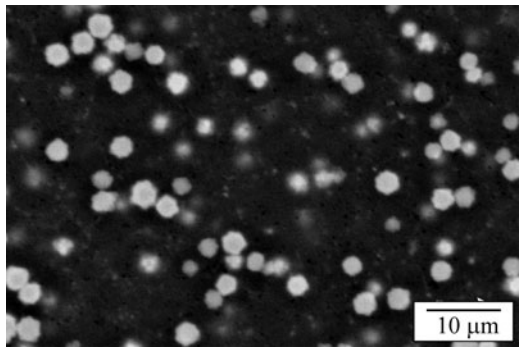

Figure 9. Backscattered electron micrograph of the alloy $Al_{92.5}Mn_3Be_{4.5}$ in the as-cast condition.

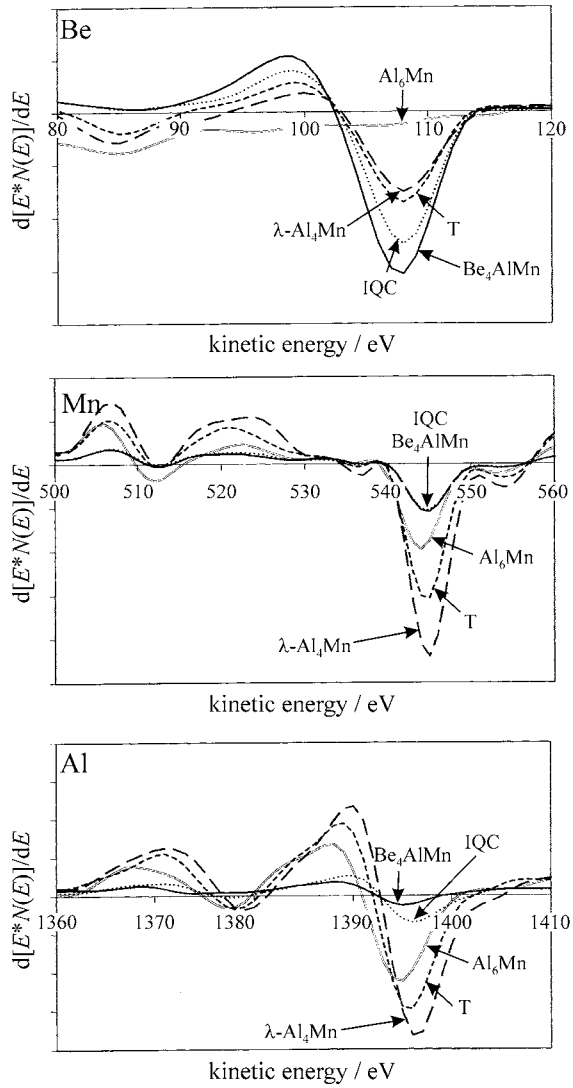

Figure 10. The derivative Auger spectra for Be, Mn, and Al in the investigated phases.

4.2:1. This is not far from the ratio 467:107, which was established by Kreiner and Franzen (1997). AES clearly revealed the presence of Be with the corresponding spectra (Fig. 10). In the $Al_{79}Mn_{17}Be_4$ alloy, the λ-Al_4Mn phase contained up to 5 at.% Be; thus all the Be present within the alloy was dissolved in this phase. λ-Al_4Mn was saturated with Be after annealing the alloy $Al_{97.3}Mn_{1.9}Be_{0.8}$ for 1 month at 600°C. Detailed quantitative AES revealed the following composition for λ-Al_4Mn:$Al_{75\pm3}Mn_{18\pm2}Be_{7\pm2}$. The sum (Al + Be) was ≈82 at.%, and the atomic ratios

Table 4. Chemical Compositions of Be_4AlMn in Different Alloys and Conditions, as Determined Using Auger Electron Spectroscopy (AES).

	Al	Mn	Be	Al/Mn	Al + Be
$Al_{97.3}Mn_{1.9}Be_{0.8}$	20.63 ± 1.087	13.65 ± 0.742	65.73 ± 1.435	1.51	86.36
$Al_{75}Mn_{15}Be_{10}$, 660°C, 1 month	25.27 ± 2.143	13.58 ± 0.035	61.17 ± 2.1	1.87	86.44
$Al_{75}Mn_{15}Be_{10}$, 750°C, 1 month	21.07 ± 0.707	16.89 ± 0.184	62.05 ± 0.516	1.25	83.12
$Al_{92.5}Mn_3Be_{4.5}$, 660°C, 1 month	25.95 ± 0.283	16.28 ± 0.283	57.77 ± 0.573	1.59	83.72
$Al_{92.5}Mn_3Be_{4.5}$, 600°C, 1 month	23.83 ± 1.52	12.41 ± 0.544	63.77 ± 2.065	1.92	87.6

(Al + Be)/Mn were close to 4.5. This could indicate that Be replaces Al atoms. The presence of Be did not alter the lattice parameters of λ-Al_4Mn significantly. The differences were only up to 1 at.% for paramater *a*, and only 0.2% for parameter *c*.

Be_4AlMn

In EDS spectra of this phase, a small but clearly resolved Be peak appeared at 0.11 keV. However, it was impossible to determine the Be content quantitatively. The atomic ratio Al:Mn was not 1:1 as expected from the chemical formula, moreover the Al content was always larger than the Mn content. Most of the alloys had an Al:Mn atomic ratio around 1.5:1, whereas the Be-rich alloy possessed a ratio closer to 1.9:1. Table 4 shows the composition of Be_4AlMn within different alloys and conditions as determined using AES. All measurements yielded the following composition for the Be_4AlMn phase: $Be_{63\pm3}Al_{23\pm3}Mn_{14\pm3}$. It is interesting to note that the composition varied only slightly, however, the ratio (Al + Be) was always close to six; similar to that in the Al_6Mn. Another notable feature was that the Be_4AlMn particles were never fully homogeneous even after 720 h at 660 and 750°C. In the backscattered electron images, this phase exhibited itself as having areas with variations in brightness. The Mn content was 2–3 at.% higher in the brighter areas. This could result from a coarsening of those nanodomains found by Boncina et al. (2009) in Be_4AlMn in the as-cast condition. The lattice parameters of Be_4AlMn deviated <0.4% from those in the crystallographic databases; thus variations of chemical composition did not have a significant effect on the size of the unit cell.

T Phase

Composition of the $Al_{75}Mn_{15}Be_{10}$ alloy corresponded with the ideal composition of the T phase discovered by Raynor et al. (1953). In the as-cast state, it was composed of not only the T phase (Fig. 7a) but even after annealing for 720 h at 660 and 750°C, it consisted of three phases: α-Al, Be_4AlMn, and T. A typical microstructure is shown in Figure 7b. Peaks of the T phase prevailed in the corresponding XRD pattern (Fig. 4). The T phase could be most reliably identified at smaller angles (Fig. 4). Namely, at low angles, the diffraction peaks of the lattice planes with the largest interplanar distances did not overlap with the peaks of other phases. The lattice parameters of the T phase deviated by only up to 0.5% from those determined by Kim et al. (2002). They determined the lattice parameters of the T phase. However, they did not provide a list of the prominent peaks that may have made identification of this phase much easier. This information is given in Table 5.

Table 5. The More Prominent Peaks of the T Phase.

h k l	*d*(*h k l*) (nm)	Relative Intensity
0 0 2	1.2317	2
0 1 1	0.9774	2
0 1 2	0.8055	9
1 1 0	0.6148	18
0 1 4	0.5335	4
0 1 2	0.5204	4
0 2 2	0.4887	19
0 2 3	0.4467	9
1 1 4	0.4351	6
0 2 4	0.4028	7
1 1 2	0.3825	14
0 2 5	0.3616	4
1 1 6	0.3414	7
1 2 4	0.3369	19
0 2 6	0.3351	3
1 2 8	0.2446	18
1 3 6	0.2397	8
2 3 4	0.2271	9
0 4 6	0.2234	23
0 1 11	0.2192	10
1 3 8	0.2131	7
1 4 5	0.2102	96
3 3 0	0.2049	28
0 1 12	0.2016	100

EDS revealed that the Al:Mn atomic ratio was within the range of 3.5:1 to 3.9:1. AES clearly confirmed the presence of Be in this phase (Fig. 10). Comparison of the AES spectra indicated that the T phase contained more Be than λ-Al_4Mn. A rigorous quantitative AES analyses within different alloys and under different heat-treated conditions indicated that this phase was stable within a rather narrow concentration range. Its composition could be written using the following chemical formula: $Al_{72\pm3}Mn_{19\pm2}Be_{9\pm2}$. It was disclosed that the T phase contained more Mn and less Be with respect to the ideal composition of $Al_{15}Mn_3Be_2$. The Al:Mn ratio lay between 3.5:1 and 3.9:1, which was similar to that determined using EDS. The atomic ratio

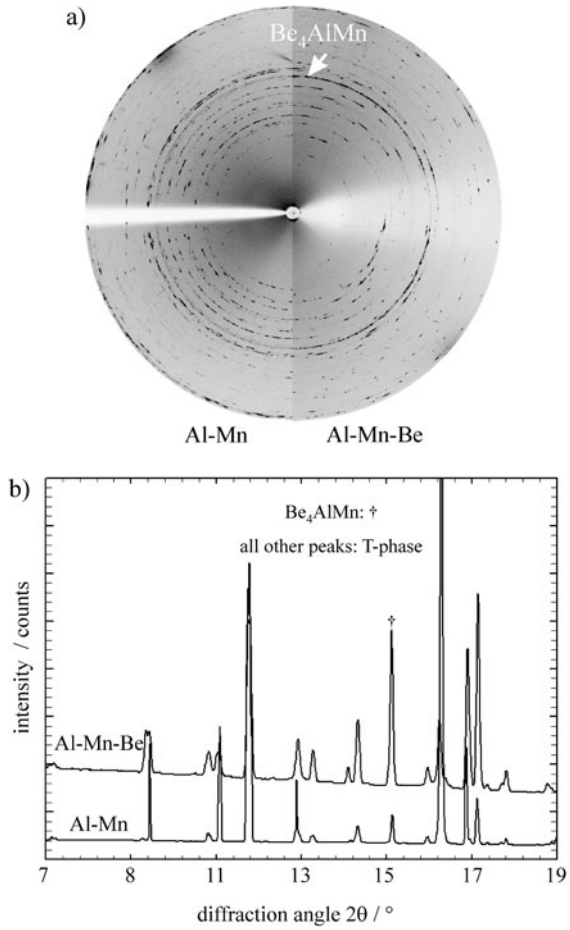

Figure 11. Comparison between two-dimensional X-ray diffraction images for binary and ternary alloys (**a**), and their integrated data (**b**).

Mn:Be was between 2:1 and 3:1, which is appreciably greater than the "ideal" 1.5:1. This phase had a similar chemical composition to that of λ-Al_4Mn; thus it could only be distinguished from it through highly accurate AES analysis. However, the diffraction peaks of both phases at lower angles lay at distinctly different positions (Fig. 4), thus XRD represents the most reliable method for distinguishing these two phases.

The XRD pattern of the T phase was compared with the XRD pattern of Al_4Mn formed within the $Al_{89}Mn_{11}$ alloy upon casting from the liquid phase (Fig. 11). A comparison between the two dimensional XRD images (Fig. 11a) revealed that the XRD data of the binary alloy (left side) matched entirely with the XRD data of the ternary alloy (right side). The integrated XRD data (Fig. 11b) showed the matching of peaks in both alloys. Any differences in peak intensities can be attributed to different grain sizes and preferential orientations of the phases. It can be inferred that the T phase in the ternary system Al–Be–Mn arises from a metastable phase in the Al–Mn system. Incorporation of Be into the structure increases its thermodynamic stability so it becomes more thermodynamically stable in Al–Mn–Be alloys, at least within the temperature range between 660 and 750°C.

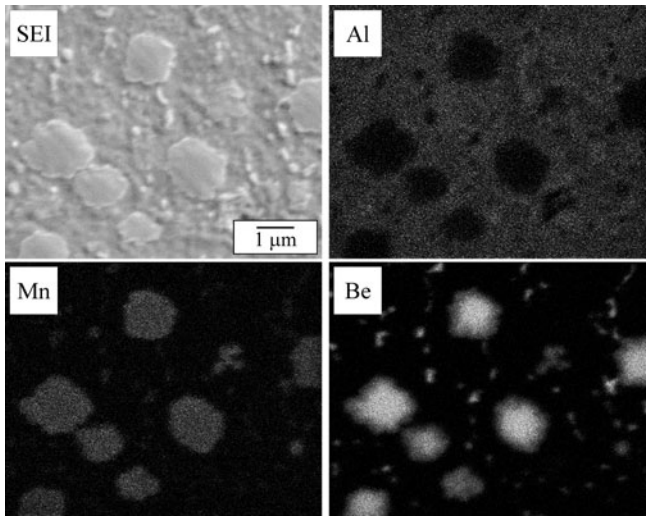

Figure 12. Auger elemental maps for Al, Mn, and Be for the alloy $Al_{92}Mn_3Be_5$ in the as-cast condition.

IQC

In Al–Mn–Be alloys, IQC forms upon rapid solidification, and after casting into thin copper moulds. Within an investigated sample, the IQC particles possessed rounded shapes (Fig. 9). They had a bimodal-size distribution. The smaller particles had diameters of around 0.1 μm, and the larger particles of up to 1 μm. The latter formed as a primary phase upon solidification, whilst the former were sectioned thin lamellae of the eutectic IQC phase. Figure 12 shows the Auger electron maps for Al, Mn, and Be. Mn was uniformly distributed within the IQC phase, whereas Be was concentrated at the centers of the particles. The content of Mn was 14 ± 2 at.% Mn. The Be content was as high as 45 ± 3 at.% Be at the centers, and 25 ± 2 at.% Be at their circumferences. The sum (Al + Be) was always ≈86 at.%, and thus the ratio (Al + Be):Mn was 6:1; the same as in the binary Al–Mn IQC phase. This strongly indicated that Be substitutes Al in this phase.

The higher Be content at the particle centers indicated that in the melt Be-rich clusters existed before solidification, perhaps close to the composition of the Be_4AlMn phase. This phase also had the sum (Al + Be) ≈86 at.%, and the ratio (Al + Be):Mn; 6:1. The Be content in the remaining liquid was reduced, and some Be was replaced by Al. Thus, the content of Be in the IQC phase decreased upon solidification.

Conclusions

Based on comprehensive examination of the Al–Be–Mn ternary system's constitution, we can conclude that

- The atomic ratio Al:Mn in Be_4AlMn was not 1:1, but varied within the range between 1.5:1 and 2:1. Its crystal structure and lattice parameters were equal to those in the crystallographic databases.
- Al_6Mn had a stoichiometric composition. Be solubility in Al_6Mn was lower than its detection limit. Its crystal struc-

ture and lattice parameters were identical to those in the crystallographic databases.

- The binary compound λ-Al_4Mn can dissolve at up to 7 ± 2 at.% Be. The atomic ratio Al:Mn was slightly higher than 4:1, and Be does not have any detectable effect on the lattice parameters of λ-Al_4Mn.
- The T phase (also known in the literature as $Al_{15}Mn_3Be_2$) contained more Mn and less Be than in the idealized formula. It contained 19 ± 2 at.% Mn and 9 ± 2 at.% Be. The metastable binary Al–Mn compound with apparently the same crystal structure as the T phase formed in $Al_{89}Mn_{11}$ alloy upon casting into a metallic mould with a cooling rate of ~10 K/s. The cumulative content of Be + Al was around 80 at.%. Be stabilizes this structure, and the T phase is thermodynamically stable at least within the temperature range between 660 and 750°C.
- An IQC phase formed upon solidification of Al–Mn–Be alloys in thin metallic moulds and by rapid solidification. It contained between 25 ± 2 and 45 ± 3 at.% Be, whereas the content of Mn was always fairly low—within a concentration range of 14 ± 2 at.% Mn. The cumulative Be + Mn content was always 86 ± 2 at.%, so its formula could be $(Al,Be)_6Mn$.

Acknowledgments

This work was partially financed by the research programme P2-0120 (Slovenian Research Agency—ARRS). Part of the work was carried out with the support of the European Community. We appreciate the support of the European Research Infrastructure EUMINAfab (funded under the FP7 specific programme Capacities, Grant Agreement Number 226460), and its partner Karlsruhe Institute of Technology (KIT). The XRD investigations at Elettra, Sincrotrone Trieste, Italy, were funded by the European Community's Seventh Framework Programme (FP7/2007-2013) under grant agreement N° 226716. The authors also wish to thank Mrs. Vesna Krapež for the metallographic preparation of the samples.

Carrabine, J.A. (1963). Ternary AlMnBe4 phases in commercially pure beryllium. *J Nucl Mater* **8**, 278–280.

Doyle, Z. & McDaniel, F.D. (2003). Auger electron spectroscopy. In *Characterisation of Materials*, Kaufmann, E.N. (Ed.), pp. 1157–1174. Hoboken, NJ: John Wiley & Sons Inc.

Goldstein, J.I., Newbury, D.E., Echlin, P., Joy, D.C., Fiori, C. & Lifshin, E. (1981). *Scanning Electron Microscopy and Microanalysis*. New York, London: Plenum Press.

Grushko, B. & Balanetskyy, S. (2008). A study of phase equilibria in the Al-rich part of the Al-Mn alloy system. *Int J Mater Res* **99**, 1319–1323.

Kim, S.H., Song, G.S., Fleury, E., Chattopadhyay, K., Kim, W.T. & Kim, D.H. (2002). Icosahedral quasicrystalline and hexagonal approximant phases in the Al-Mn-Be alloy system. *Philos Mag A* **82**(8), 1495–1508.

Kreiner, G. & Franzen, H.F. (1997). The crystal structure of lambda-Al4Mn. *J Alloy Compd* **261**(1–2), 83–104.

Markoli, B., Boncina, T. & Zupanic, F. (2012). Behaviour of a quasicrystalline strengthened Al-alloy during compression testing. *Materialwiss Werkstofftech* **43**(4), 340–344.

McAlister, A. & Murray, J. (1990). Al-Mn (aluminum-manganese). In *Binary Alloy Phase Diagrams*, Massalski, T. (Ed.), pp. 171–174. Materials Park, OH: ASM International.

Murray, J. & Kahan, D. (1990). Al-Be (aluminum-beryllium). In *Binary Alloy Phase Diagrams*, Massalski, T. (Ed.), pp. 125–127. Materials Park, OH: ASM International.

Okamoto, H. & Tanner, L. (1990). Be-Mn (beryllium-manganese). In *Binary Alloy Phase Diagrams*, Massalski, T. (Ed.), pp. 665–667. Materials Park, OH: ASM International.

Pan, Z., Du, Y., Huang, B.Y., Liu, Y. & Wang, R.C. (2004). A thermodynamic description of the Al-Be system: Modeling and experiment. *Calphad-Comput CouplingPhase Diagrams Thermochem* **28**(4), 371–378.

Raynor, G.V., Faulkner, C.R., Noden, J.D. & Harding, A.R. (1953). Ternary alloys formed by aluminium, transitional metals and divalent metals. *Acta Metall* **1**, 629–648.

Shukla, A. & Pelton, A. (2009). Thermodynamic assessment of the Al-Mn and Mg-Al-Mn systems. *J Phase Equilib Diffus* **30**(1), 28–39.

Trambly de Laissardière, G., Nguyen-Manh, D. & Mayou, D. (2005). Electronic structure of complex Hume-Rothery phases and quasicrystals in transition metal aluminides. *Prog Mater Sci* **50**(6), 679–788.

Zupanic, F., Markoli, B., Naglic, I. & Boncina, T. (2013). The experimental investigation of phase equilibria in the Al-rich corner within the ternary Al-Mn-Be system. *J Alloys Compd* **570**, 125–132.